Wide-Field Dynamic Magnetic Microscopy Using Double-Double Quantum Driving of a Diamond Defect Ensemble

Zeeshawn Kazi,[1,*] Isaac M. Shelby,[1] Hideyuki Watanabe,[2] Kohei M. Itoh,[3,4] Vaithiyalingam Shutthanandan,[5] Paul A. Wiggins,[1,6] and Kai-Mei C. Fu[1,7]

[1] *Physics Department, University of Washington, Seattle, Washington 98105, USA*

[2] *Nanoelectronics Research Institute, National Institute of Advanced Industrial Science and Technology, Tsukuba Central 2, 1-1-1 Umezono Tsukuba, Ibaraki 305-8568, Japan*

[3] *Spintronics Research Center, Keio University, 3-14-1 Hiyoshi, Kohoku-ku, Yokohama 223-8522, Japan*

[4] *School of Fundamental Science and Technology, Keio University, 3-14-1 Hiyoshi, Kohoku-ku, Yokohama 223-8522, Japan*

[5] *Environmental and Molecular Sciences Laboratory, Pacific Northwest National Laboratory, Richland, Washington 99352, USA*

[6] *Bioengineering Department, University of Washington, Seattle, Washington 98105, USA*

[7] *Electrical and Computer Engineering Department, University of Washington, Seattle, Washington 98105, USA*

(Received 18 February 2020; revised 15 January 2021; accepted 6 April 2021; published 14 May 2021)

Wide-field magnetometry can be realized by imaging the optically detected magnetic resonance of diamond nitrogen-vacancy (N-V) center ensembles. However, N-V ensemble inhomogeneities significantly limit the magnetic field sensitivity of these measurements. We demonstrate a double-double quantum (DDQ) driving technique to facilitate wide-field magnetic imaging of dynamic magnetic fields at a micron scale. DDQ imaging employs four-tone radio-frequency pulses to suppress inhomogeneity-induced variations of the N-V resonance response. As a proof of principle, we use the DDQ technique to image the dc magnetic field produced by individual magnetic nanoparticles tethered by single DNA molecules to a diamond-sensor surface. This demonstrates the efficacy of the diamond N-V ensemble system in high-frame-rate magnetic microscopy, as well as single-molecule biophysics applications.

DOI: 10.1103/PhysRevApplied.15.054032

I. INTRODUCTION

The success of the negatively charged nitrogen-vacancy (N-V) center in diamond for magnetic field sensing is due to a powerful combination of characteristics: a long spin-coherence time, the ability to perform optically detected magnetic resonance (ODMR) spectroscopy at room temperature, and a solid-state host environment that facilitates sample-sensor integration [1–4]. One exciting emerging application is magnetic field imaging using a diamond sensor comprising a diamond substrate with a thin layer of N-V centers fabricated at the top surface [5–9]. In this N-V ensemble imaging system, it is critical that the inhomogeneities across the imaging area are eliminated in order to reach the sensitivity floor given by a single-pixel resonance curve. To this end, the N-V community has demonstrated many sensor growth and fabrication methods that increase the N-V density and homogeneity [10–15], as well as quantum control methods that suppress external-field dependence and increase ensemble spin coherence [16–19]. In this paper, we expand on these techniques to present a quantum control method compatible with high-frame-rate magnetic field imaging. Our method, double-double quantum (DDQ) driving, mitigates inhomogeneities caused by variations of the N-V resonance curve.

In N-V ensemble ODMR, magnetic fields can be imaged by characterizing the photoluminescence of optically excited N-V centers after probing the N-V spin ground states with radio-frequency (rf) π pulses [Fig. 1]. The resonance radio frequency depends on the magnetic field because of the Zeeman splitting of the $|m_s = \pm 1\rangle$ N-V electronic spin states [1]. However, in addition to sensitivity to the magnetic field, the resonances are also perturbed by inhomogeneities in the electric field, the temperature, and the crystal strain [20–23]. Due to the symmetry of the N-V center, these nonmagnetic perturbations affect the two N-V electron spin resonances ($|m_s = 0\rangle \leftrightarrow |m_s = \pm 1\rangle$) in the same way and can be eliminated by characterizing both resonances [18,24].

For wide-field magnetic imaging of time-varying fields, the full characterization of the resonance curves is too slow to capture the magnetic field dynamics in many

*zeeshawn@uw.edu

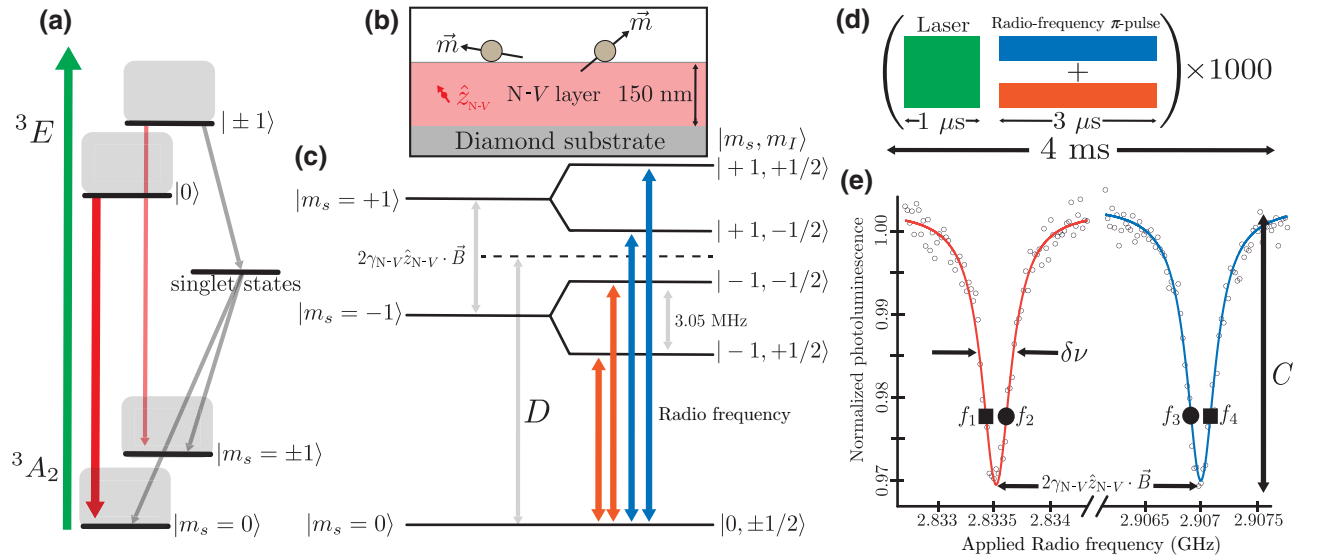

FIG. 1. Wide-field pulsed magnetic imaging using an N-V ensemble. (a) The N-V electronic-energy-level diagram, showing the ground, excited spin states ($|m_s = 0\rangle$,$|m_s = \pm 1\rangle$), singlet states, optical excitation (green arrow), emitted photoluminescence (red arrows), and spin-selective nonradiative intersystem crossing (gray arrows). (b) A schematic showing 50-nm ferromagnetic nanoparticles adhered to the diamond surface. The magnetic moments of the particles are oriented randomly. The 150-nm N-V layer (pink) is fabricated on top of the diamond substrate (gray) and a single N-V pointed along the (111) orientation is shown (red). (c) The N-V ground-state energy-level diagram, showing the zero-field splitting (D), Zeeman splitting of the $|m_s = \pm 1\rangle$ states ($2\gamma_{N\text{-}V}\hat{z}_{N\text{-}V} \cdot \vec{B}$), and ^{15}N–N-$V$ hyperfine splitting (3.05 MHz). The rf excitation (orange and blue arrows) rotates the N-V spin between the $|m_s = 0\rangle$ and $|m_s = \pm 1\rangle$ states. Two-tone rf excitation is simultaneously driven over the two ^{15}N-N–V hyperfine transitions to produce a single combined resonance for each N-V electron spin state ($|m_s = \pm 1\rangle$). (d) Laser and multitone rf π pulses are repeated throughout the camera exposure to facilitate wide-field imaging. (e) A Lorentzian-shaped reduction in N-V PL is observed when a rf scan is performed through each spin-transition frequency. The resonances are Zeeman split by the external magnetic field. The outer (inner) inflection points f_1,f_4 (f_2,f_3) are denoted by black squares (circles). For the resonance curves shown, the FWHM line width $\delta\nu = 300$ kHz and fractional optical contrast $C = 0.03$, with optical pulse = 500 ns, rf pulse = 3500 ns, photon collection rate = 1.1×10^7 Hz from a 1 μm^3 pixel (0.15 μm^3 voxel), and integration time per data point = 144 ms.

applications. In these dynamic applications, shifts of one resonance curve can instead be mapped to changes in the emitted N-V photoluminescence (PL) intensity by applying single-frequency rf excitation [25–27]. This "single quantum" (SQ) imaging modality enables partial reconstruction of the local magnetic field with a higher frame rate. The double quantum (DQ) modality, which drives both N-V electron spin transitions simultaneously by applying a two-tone rf pulse, eliminates pixel-to-pixel nonmagnetic perturbations of the transition resonance frequencies [18,24]. However, variations of the shape of the resonance curve also cause changes in the emitted PL intensity and therefore generate spurious contrast, which limits the magnetic sensitivity. These variations arise from inhomogeneities in N-V and other paramagnetic spin densities as well as external fields [16] and, as shown in this work, can severely limit the utility of the DQ modality for wide-field imaging applications. By expanding to a four-tone DDQ driving scheme, we suppress anomalous contrast due to resonance-curve-shape variations pixel by pixel across the field of view. This enables high-frame-rate imaging of time-dependent magnetic fields. We first demonstrate the SQ, DQ, and DDQ imaging modalities by imaging static fields and show that the DDQ signal is linearly proportional to the magnetic field projection along the N-V symmetry axis. We then use the DDQ driving technique to image the dynamic magnetic field produced by a ferromagnetic nanoparticle tethered by a single DNA molecule to the diamond-sensor surface.

II. EXPERIMENTAL METHODS

The wide-field N-V magnetic particle imaging (magPI) platform used in this work utilizes a diamond sensor with a near-surface high-density N-V ensemble [Fig. 1(b)]. A 150-nm^{15} N doped isotope-purified (99.999% ^{12}C) layer is grown by chemical-vapor deposition on an electronic-grade diamond substrate (Element Six). The sample is implanted with 25-keV He^+ at a dose of 5×10^{11} ions/cm^2 to form vacancies, followed by a vacuum anneal at 900 °C for 2 h for N-V formation and an anneal in O_2 at 425 °C for 2 h for charge-state stabilization [15]. The resulting ensemble has N-V density of 1.7×10^{16} cm^{-3} and ensemble spin

coherence time $T_2^* = 2.5\ \mu$s (further details are given in the Supplemental Material [28]).

The N-V electronic structure and optical and rf control are summarized in Fig. 1. A 532-nm laser pulse is used to optically pump the N-V ensemble into the $|m_s = 0\rangle$ triplet ground state. The rf excitation drives transitions from this ground state into the $|m_s = \pm 1\rangle$ spin states. Optical excitation from the $|m_s = \pm 1\rangle$ states results in a reduction of the PL intensity due to a spin-selective nonradiative intersystem crossing [29]. This relaxation provides the spin-dependent PL contrast and initialization into the $|m_s = 0\rangle$ state. The monitoring of the emitted PL as a function of the radio frequency enables measurement of ODMR for each N-V ground-state spin transition [Fig. 1(e)].

From a Lorentzian-shaped resonance curve [see Fig. 1(e)], the volume-normalized shot-noise-limited dc magnetic sensitivity is given by

$$\eta_{\mathrm{SQ}}^{V} \approx \frac{1}{\gamma_{\text{N-}V}} \frac{\delta\nu}{C} \sqrt{\frac{V}{N}}, \tag{1}$$

where C is the optical contrast (the fractional depth of the resonance curve), $\delta\nu$ is the full-width-at-half-maximum (FWHM) line width, $\gamma_{\text{N-}V}$ is the N-V gyromagnetic ratio (28 MHz/mT), N is the photon detection rate, and V is the collection volume [1]. In the magPI platform, the average volume normalized sensitivity $\eta_{\mathrm{SQ}}^{V} \approx 31\ \mathrm{nT\,Hz^{-1/2}}\ \mu\mathrm{m}^{3/2}$. All three sensor parameters, $C, \delta\nu$, and N, vary across the imaging field of view.

Optical power broadening of the resonance curve is eliminated by using pulsed excitation, in which optical and rf fields are applied separately [30]. Optical pulses and rf π pulses (both microsecond-scale) are applied to the ensemble repeatedly to fill a scientific CMOS camera exposure (millisecond-scale). Each camera exposure is taken with a single set of radio frequencies with a fixed pulse duration [Fig. 1(d)], enabling pulsed N-V ensemble control and readout with wide-field camera exposure times [31].

The rf excitation is delivered via a broadband microwave antenna with transmission resonance at the N-V zero-field splitting D [32]. Each radio frequency applied is mixed to create two equal tones separated by 3.05 MHz, which enables simultaneous driving of the two ^{15}N–N-V hyperfine transitions [33] [Fig. 1(c)] and produces one combined resonance for each $|m_s = 0\rangle \leftrightarrow |m_s = \pm 1\rangle$ transition [Fig. 1(e)]. Samarium cobalt ring magnets (SuperMagnetMan) are used to apply a 1-mT static external magnetic field along the (111) N-V orientation ($\hat{z}_{\text{N-}V}$). More details about the experimental setup can be found in the Supplemental Material [28].

We first use the magPI platform to image the static dipolar magnetic field produced by a 50-nm dextran-coated $CoFe_2O_4$ ferromagnetic nanoparticle (micromod Partikeltechnologie) deposited and dried onto the diamond-sensor surface [Fig. 1(b)]. These biocompatible particles produce nanoscale magnetic fields that lie in the dynamic range of the N-V sensing ensemble defined by the $\delta\nu$ of the resonance curves. For other imaging applications, the sensor dynamic range can be increased at the expense of the magnetic sensitivity by rf broadening the resonance curve.

We then demonstrate dynamic magnetic imaging using the DDQ technique on a tethered-particle-motion (TPM) assay [34], in which 500-nm streptavidin-coated ferromagnetic nanoparticles (micromod Partikeltechnologie 05-19-502) are tethered by 940-bp single DNA molecules to the diamond surface. The diamond-DNA-particle tethering protocol follows Ref. [35]. Fluid that is flowed through the sample chamber alters the orientation of the nanoparticle magnetic moment and the changing magnetic field is imaged at a high frame rate.

III. STATIC MAGNETIC IMAGING MODALITY

To measure static fields, the full N-V resonance curve can be measured in wide field with arbitrarily long acquisition times. Taking a series of PL images over a range of radio frequencies allows fitting of the entire resonance response in the measured range. Mapping the fitted resonance frequency at each pixel results in a partial reconstruction of the magnetic field, as seen in Fig. 2(a). Taking the difference between the $|m_s = 0\rangle \leftrightarrow |m_s = \pm 1\rangle$ resonance-frequency maps eliminates shifts of the resonance due to fields other than the magnetic field and enables imaging of the absolute magnetic field projection along the N-V symmetry axis [36], as seen in Fig. 3(a).

For quickly varying magnetic fields, imaging via the static magnetic imaging procedure may not be possible. We thus require a dynamic imaging modality that reproduces the absolute magnetic field across the imaging field of view without prior per-pixel calibration and is compatible with high-frame-rate imaging.

IV. DYNAMIC MAGNETIC IMAGING MODALITIES

A. SQ difference imaging

The simplest dynamic imaging modality uses rf excitation applied at one inflection point of one of the N-V resonance curves [Fig. 1(e)]. PL images taken with rf π pulses applied are subtracted from PL images taken without radio frequency to detect changes in emitted N-V PL [27]. We define a SQ difference image (DI) as

$$S_{\mathrm{SQ}}(f_1) = \frac{I_{\mathrm{off}} - I_{\mathrm{on}}(f_1)}{I_{\mathrm{off}}}, \tag{2}$$

in which $I_{\mathrm{on}}(f_1)$ is the intensity image taken with applied rf π pulses at f_1 and I_{off} is the image taken with no applied radio frequency. We assume that the N-V ensemble is operating in the linear-response regime of the resonance curve,

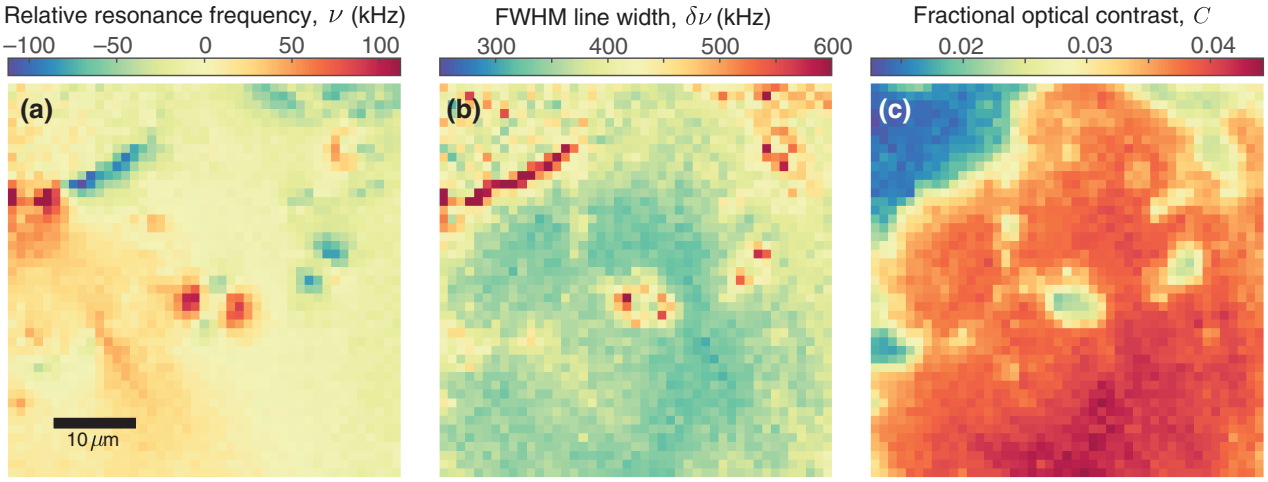

FIG. 2. Multiple mechanisms lead to changes in N-V ODMR on a micron scale when imaging static magnetic dipole and strain fields. (a) The resonance-frequency ν shifts due to the magnetic field and the crystal strain. (b) The FWHM line width $\delta\nu$ varies due to the gradients of the magnetic and strain fields that inhomogeneously broaden the N-V ODMR in each pixel. (c) The optical contrast C also varies due to inhomogeneous broadening of the N-V ODMR.

i.e., $\gamma_{\text{N-}V}\hat{z}_{\text{N-}V}\cdot\vec{B} < \delta\nu$. The per-pixel signal is then given by

$$S_{\text{SQ}}^{\text{pp}}(f_1) = \frac{9}{8}C - \frac{3\sqrt{3}}{4}\frac{C}{\delta\nu}[\nu(\vec{E},\vec{B},T,\ldots) - f_1]. \quad (3)$$

As discussed above, the resonance frequency ν depends on the magnetic field $\vec{B}$ and also varies with local electric field $\vec{E}$, the temperature T, and the crystal strain.

Additionally, variations in curve shape, and thus C [Fig. 2(b)] and $\delta\nu$ [Fig. 2(c)], cause variations of the resonance-curve inflection point, contributing to the SQ signal. Microscopic and mesoscopic strain inhomogeneities result in inhomogeneous broadening of the resonance curve [8]. Also, dephasing due to dipolar interactions between sensing N-V centers and other paramagnetic impurities (e.g., P1 and N-V) fundamentally limit the N-V ensemble coherence and, thus, the ODMR line width [15,16].

The SQ DI enables imaging of some nanoscale magnetic structure but the sensitivity of this technique is limited. In Fig. 3(b), we show a SQ DI image, with its corresponding static magnetic field map in Fig. 3(a). The SQ DI enables partial mapping of the magnetic field projection but is limited by contributions to the resonance-frequency shift by strain gradients, as seen in the SQ-signal-color gradient from upper left to lower right in Fig. 3(b).

B. DQ difference imaging

The temperature, electric field, and strain shift the zero-field splitting of the N-V ground state, causing common-mode shifts of the $|m_s = 0\rangle \leftrightarrow |m_s = \pm 1\rangle$ transitions [5]. Conversely, the magnetic-field-induced Zeeman effect splits the two transitions. Thus, by probing the difference of the two transition resonance frequencies, the common-mode shifts can be subtracted out and the magnetic field projection can be measured directly. We use a DQ driving scheme [17,24], applying two-tone rf π pulses at the opposite inflection points of the two resonance curves simultaneously [Fig. 1(e)]. We construct a DQ DI by subtracting the PL image taken with DQ rf driving from an image taken with no radio frequency applied:

$$S_{\text{DQ}}(f_1,f_4) = \frac{I_{\text{off}} - I_{\text{on}}(f_1,f_4)}{I_{\text{off}}}, \quad (4)$$

in which $I_{\text{on}}(f_1,f_4)$ is the image taken with applied rf π pulses at f_1 and f_4 simultaneously and I_{off} is the image taken with no applied radio frequency. We again assume a linear response of the resonance curves and additionally assume that the two resonance curves have the same shape (see the Supplemental Material [28]). The per-pixel DQ signal is

$$S_{\text{DQ}}^{\text{pp}}(f_1,f_4) \approx \frac{9}{4}C - \frac{3\sqrt{3}}{4}\frac{C}{\delta\nu}(f_1 - f_4) - \frac{3\sqrt{3}}{4}\frac{C}{\delta\nu}(2\gamma_{\text{N-}V}\hat{z}_{\text{N-}V}\cdot\vec{B}). \quad (5)$$

By defining $\langle\vec{B}\rangle$ as the average magnetic field over the imaging field of view, Eq. (5) simplifies to

$$S_{\text{DQ}}^{\text{pp}}(f_1,f_4) = \frac{9}{4}C + \frac{3\sqrt{3}}{4}\frac{C}{\delta\nu}2\delta_0 - \frac{3\sqrt{3}}{4}\frac{C}{\delta\nu}\left[2\gamma_{\text{N-}V}\hat{z}_{\text{N-}V}\cdot\left(\vec{B} - \langle\vec{B}\rangle\right)\right], \quad (6)$$

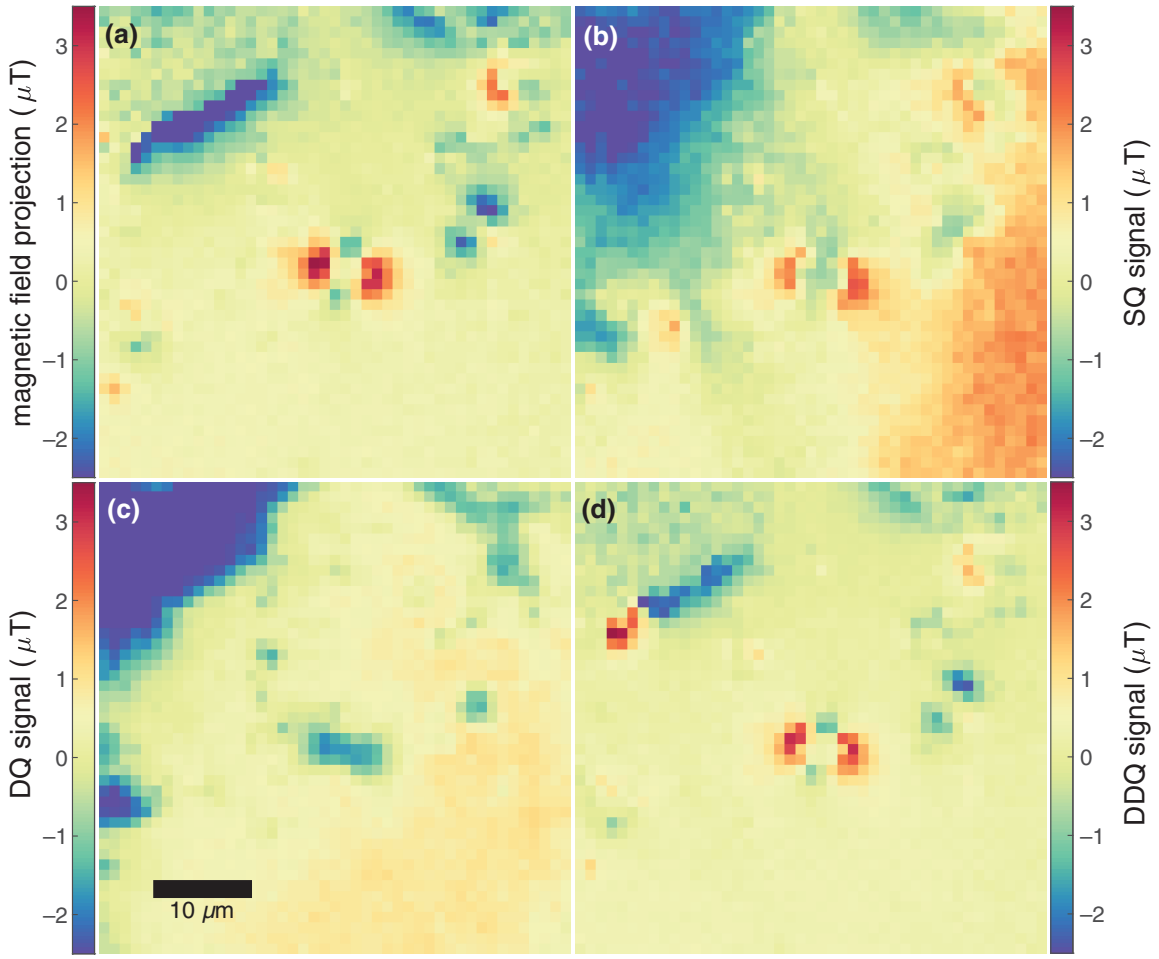

FIG. 3. Competing magnetic imaging modalities. (a) The "true" static magnetic field projection map generated with the frequency-scanning technique outlined in Sec. III (acquisition time 12 s). (b) SQ difference imaging (2.4 s). The signal measured with the SQ DI modality is a convolution of the magnetic and strain fields, which are impossible to separate with a single measurement. (c) DQ difference imaging (2.4 s). While the DQ DI modality has reduced the impact from the fields that homogeneously shift the N-V centers, the DQ signal is more sensitive to the local contrast and line-width variations of the N-V sensing curves. (d) DDQ difference imaging (2.4 s). An inspection of the competing dynamic imaging schemes (b)–(d) reveals that both the SQ (b) and DQ (c) schemes are significantly compromised by spurious contrast caused by strain gradients and curve-shape variation, respectively, while the DDQ scheme (d) faithfully approximates the "true" magnetic field projection (a) with a decreased acquisition time.

where $2\delta_0 = (f_4 - f_1) - 2\gamma_{\text{N-}V}\hat{z}_{\text{N-}V} \cdot \langle\vec{B}\rangle$. By applying f_1 and f_4 at the outer inflection points of the N-V resonance curves simultaneously [Fig. 1(e)], intensity changes induced by nonmagnetic common-mode shifts are cancelled out, while splittings caused by magnetic signal result in a sum of changes in the PL intensity. Hence, for constant C and $\delta\nu$, the DQ DI technique enables absolute magnetic imaging [24].

Although the contribution of strain-induced resonance shifts to the imaging has been eliminated, overcoming the sensitivity limits of the SQ DI, we demonstrate that DQ DI has *increased* the effect of variations in curve shape on the magnetic imaging. More specifically, variations of C and $\delta\nu$ still cause perturbations of the first two terms in Eq. (6). This effect can be seen by comparing the map of C in Fig. 2(c) to the DQ DI in Fig. 3(c). Thus, for practical applications of the DQ method to wide-field imaging, we find that curve-shape variations dominate and the DQ DI [Fig. 3(c)] is ineffective at reproducing a map of the magnetic field projection [Fig. 3(a)].

C. DDQ difference imaging

To suppress the imaging dependence on curve shape, we apply bias radio frequencies on either side of the resonance curves [37]. We construct a DDQ DI as follows:

$$S_{\text{DDQ}} = 2\frac{I_{\text{on}}(f_1,f_4) - I_{\text{on}}(f_2,f_3)}{I_{\text{on}}(f_1,f_4) + I_{\text{on}}(f_2,f_3)}, \tag{7}$$

where $I_{\text{on}}(f_1,f_4)$ $[I_{\text{on}}(f_2,f_3)]$ is the image taken with radio frequency applied at the outer (inner) inflection points of the two resonance curves simultaneously, as shown in

Fig. 1(e). By applying DQ bias radio frequencies on either side of the resonance curves, the effects of variations in the shape of the ODMR curve and the external nonmagnetic fields are mitigated. Here, the DDQ DI signal is normalized by dividing by the mean of the individual DQ frames $I_{\mathrm{on}}(f_i, f_j)$.

Because of the choice of radio frequency, the per-pixel DDQ signal simplifies in a similar manner as the DQ signal in Eq. (6), giving

$$S_{\mathrm{DDQ}}^{\mathrm{pp}} \approx \frac{3\sqrt{3}}{2}\frac{C}{\delta\nu}\left[2\gamma_{\text{N-}V}\hat{z}_{\text{N-}V}\cdot\left(\vec{B}-\langle\vec{B}\rangle\right)\right]. \tag{8}$$

DDQ eliminates the first two terms of the DQ DI signal Eq. (6) to obtain a single term that is linearly proportional to $(\vec{B}-\langle\vec{B}\rangle)$. There is still multiplicative dependence on C and $\delta\nu$ but because the shift of the resonance frequency far ($> 1\ \mu$m) from magnetic field sources falls off faster than the impact of spatial variations of curve shape due to inhomogeneous broadening, there is no DDQ signal generated in regions with no magnetic field. The DDQ DI completely eliminates the large-scale nonmagnetic gradients in the SQ DI [Fig. 3(b)] and suppresses the C and $\delta\nu$ dependence [Figs. 2(b) and 2(c)] of the DQ DI [Fig. 3(c)]. As shown in Fig. 3(d), DDQ DI provides a magnetic sensitivity similar to that of the static magnetic projection map in Fig. 3(a), with a greater than fourfold acquisition-time reduction. The static imaging modality requires enough images to fit both resonance curves; the DDQ modality instead extracts the magnetic field dependence of the resonances with only two images: $I_{\mathrm{on}}(f_1, f_4)$ and $I_{\mathrm{on}}(f_2, f_3)$. While the integration time of the DDQ image shown in Fig. 3(d) is chosen to match the signal-to-noise ratio of the magnetic field map in Fig. 3(a), DDQ enables even faster magnetic imaging as demonstrated in the next section.

We emphasize the general conditions for applicability for the DDQ method: (i) the resonance-curve shapes of the two N-V spin transitions used must be matched by driving each transition with equal Rabi frequency, (ii) nonmagnetic inhomogeneities across the imaging field of view must be smaller than the resonance FWHM line width in order to be suppressed, and (iii) sensor operation is in the linear regime, i.e., the magnetic signals to be imaged are smaller than the resonance FWHM line width. We discuss errors associated with condition (i) in the Supplemental Material [28] and note that criteria (ii) and (iii) are prerequisites for any intensity-based wide-field magnetic imaging involving N-V ensembles.

V. WIDE-FIELD DYNAMIC MAGNETIC MICROSCOPY

To demonstrate that DDQ difference imaging can facilitate high-frame-rate imaging of dynamic fields, we image the changing magnetic field produced by a ferromagnetic nanoparticle tethered to the diamond-sensor surface by a single DNA molecule. The approximate diamond-particle distance is 400 nm. Figure 4(a) shows an 8-s time-averaged

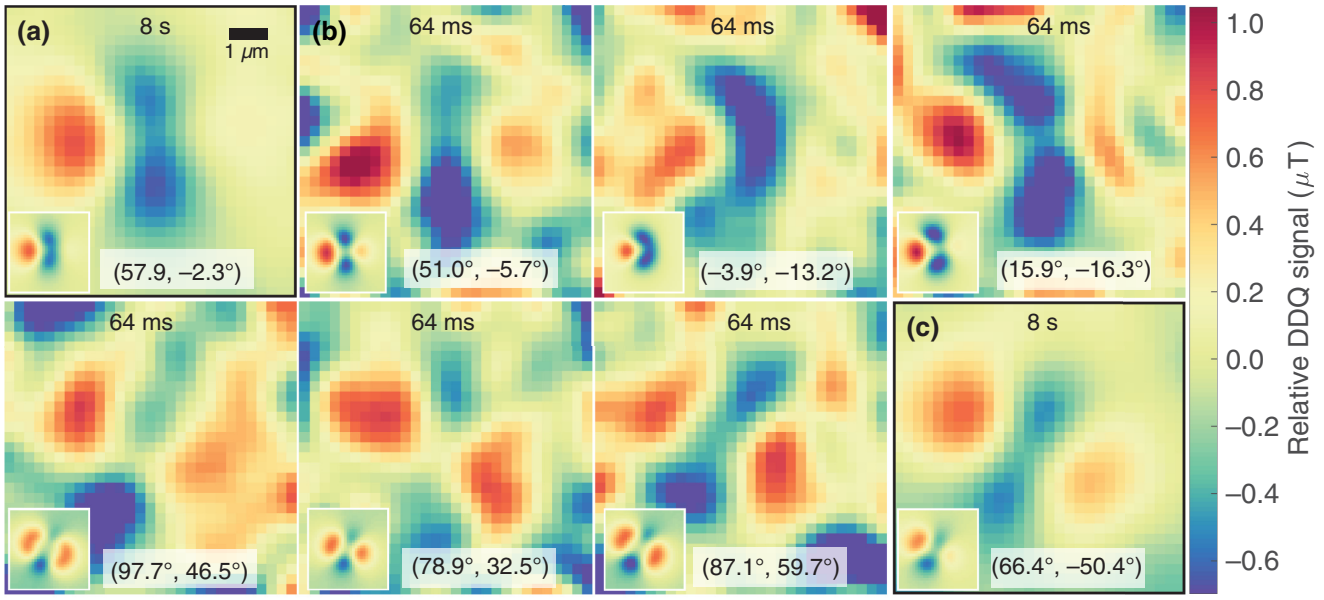

FIG. 4. DDQ imaging of the reorientation of a DNA-tethered magnetic nanoparticle under applied flow. In each panel, the observed DDQ image is compared with a fitted DDQ image (inset) to estimate the magnetic nanoparticle dipole orientation (θ, ϕ), where the N-V ensemble symmetry axis is (54.735°, 0°). For all DDQ DI in this figure, a Gaussian smoothing filter with $\sigma = 533$ nm is applied. (a) A time-averaged DDQ DI (8 s) showing the initial magnetic nanoparticle orientation before flow. (b) Representative DDQ frames (64 ms of exposure) showing nanoparticle reorientation in response to an applied flow. (c) A time-averaged DDQ DI (8 s) showing the final magnetic nanoparticle orientation with applied flow.

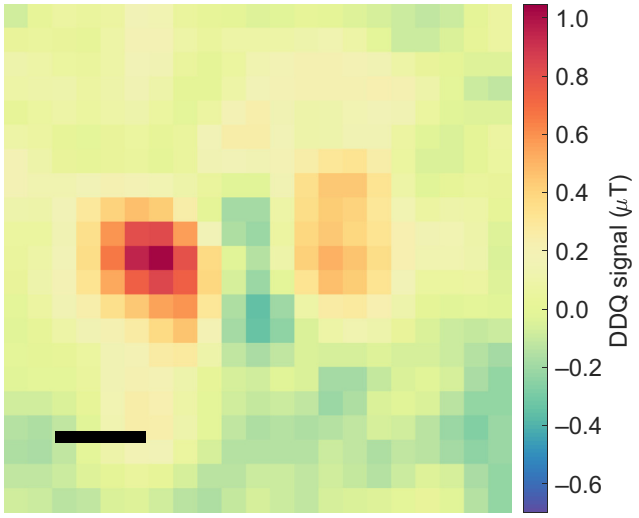

Video 1. A dynamic wide-field microscopy video (3.9 Hz) captured using the DDQ technique. The magnetic nanoparticle reorientation highlighted in Fig. 4 is shown at a slower frame rate (256-ms frames) for ease of viewing. (Scale bar = 2 μ m).

image of the field produced by the magnetic nanoparticle. A preferred direction is observed due to the partial alignment of the ferromagnetic nanoparticle moment orientation to the 0.35-mT external magnetic field, oriented along $(\theta, \phi) = (54.735°, 0°)$. Next, phosphate-buffered-saline is pulled from a reservoir through the sample channel by a syringe pump at 4 ml/min. The fluid flow exerts a hydrodynamic force and torque on the tethered-particle, causing it to reorient, changing the magnetic field at the diamond-sensor surface. Figure 4(b) displays characteristic frames, in chronological order, showing time-resolved imaging of

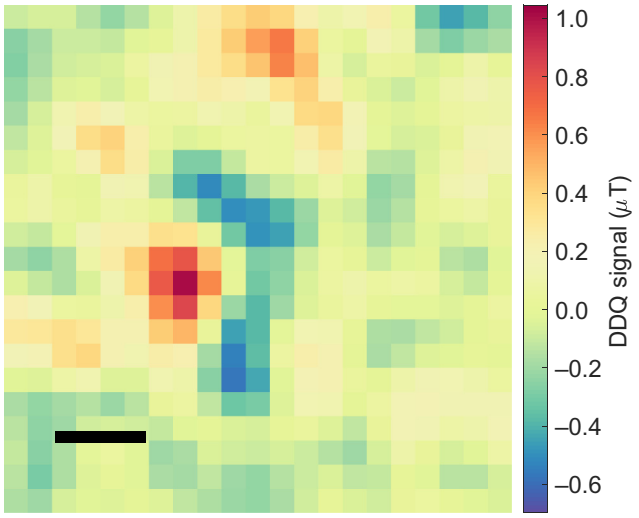

Video 2. A dynamic wide-field microscopy video (15.6 Hz) captured by the DDQ technique, with the same frame rate as Fig. 4 (64-ms frames). (Scale bar = 2 μ m).

the nanoparticle moment reorientation at a 15.6-Hz frame rate (64 ms per frame), with insets showing fitted DDQ images displaying the changing magnetic moment direction in each frame. The fluid-flow steady-state nanoparticle orientation is imaged with an 8-s-time-averaged DDQ image in Fig. 4(c). The full dynamic magnetic imaging video is shown at 3.9 Hz in Video 1 and 15.6 Hz in Video 2. This experiment represents the application of diamond-based micron-scale dynamic magnetometry to a single-molecule biological system.

VI. CONCLUSIONS AND OUTLOOK

Although the N-V community has made significant progress toward eliminating inhomogeneities in N-V ensemble-based-sensors through advanced N-V fabrication [10], quantum control methods can significantly increase the sensitivity of these systems for magnetometry applications [16]. However, existing wide-field schemes fail to reliably image magnetic fields due to micron-scale variation in the resonance-curve shape. Here, we introduce a quantum control technique, DDQ difference imaging, that is suitable for mitigating inhomogeneities in wide-field dc magnetometry to enable imaging of time-varying fields. Using four-tone rf pulses and only a two-image sequence, we show both theoretically and experimentally that DDQ difference imaging not only mitigates nonmagnetic perturbations of the N-V resonance frequency but also variations of the resonance-curve shape. Static-field imaging reveals that these resonance-shape variations can be the dominant source of imaging noise in a state-of-the-art N-V magnetic imaging surface. Finally, we use the DDQ technique to perform wide-field magnetic microscopy of a dynamic biological system, enabling high-frame-rate orientation imaging of a magnetic nanoparticle tethered to the diamond sensor by a single DNA molecule. DDQ difference imaging eliminates the need for per-pixel calibration and enables high-frame-rate magnetic microscopy via N-V photoluminescence intensity imaging.

ACKNOWLEDGMENTS

This material is based on work supported by the National Science Foundation under Grant No. 1607869. The helium-ion implantation measurements were carried out at the Environmental and Molecular Sciences Laboratory, a national scientific user facility sponsored by the Department of Energy (DOE) Office of Biological and Environmental Research and located at Pacific Northwest National Laboratory (PNNL). PNNL is a multiprogram laboratory operated for the DOE by Battelle under Contract No. DE-AC05-76RL01830. K.M.I. acknowledges support from the Spintronics Research Network of Japan.

Note added.—During the revision process, we have become aware of work demonstrating a similar technique

with similar conditions of applicability to mitigate wide-field inhomogeneities in N-V magnetic microscopy [38]. In relation to this work, our technique utilizes a simpler two-image (versus four-image) scheme, requires no phase control of the rf excitation, uses lower rf power, and is used to perform dynamic magnetic imaging.

[1] E. Abe and K. Sasaki, Tutorial: Magnetic resonance with nitrogen-vacancy centers in diamond—Microwave engineering, materials science, and magnetometry, J. Appl. Phys. **123**, 161101 (2018).

[2] S. Hong, M. S. Grinolds, L. M. Pham, D. Le Sage, L. Luan, R. L. Walsworth, and A. Yacoby, Nanoscale magnetometry with NV centers in diamond, MRS Bull. **38**, 155 (2013).

[3] R. Schirhagl, K. Chang, M. Loretz, and C. L. Degen, Nitrogen-vacancy centers in diamond: Nanoscale sensors for physics and biology, Annu. Rev. Phys. Chem. **65**, 83 (2014).

[4] G. Balasubramanian, P. Neumann, D. Twitchen, M. Markham, R. Kolesov, N. Mizuochi, J. Isoya, J. Achard, J. Beck, J. Tissler, V. Jacques, P. R. Hemmer, F. Jelezko, and J. Wrachtrup, Ultralong spin coherence time in isotopically engineered diamond, Nat. Mater. **8**, 383 (2009).

[5] E. V. Levine, M. J. Turner, P. Kehayias, C. A. Hart, N. Langellier, R. Trubko, D. R. Glenn, R. R. Fu, and R. L. Walsworth, Principles and techniques of the quantum diamond microscope, Nanophotonics **8**, 1945 (2019).

[6] J. P. Tetienne, N. Dontschuk, D. A. Broadway, A. Stacey, D. A. Simpson, and L. C. Hollenberg, Quantum imaging of current flow in graphene, Sci. Adv. **3**, 1602429 (2017).

[7] J. F. Barry, M. J. Turner, J. M. Schloss, D. R. Glenn, Y. Song, M. D. Lukin, H. Park, and R. L. Walsworth, Optical magnetic detection of single-neuron action potentials using quantum defects in diamond, PNAS **113** 14133 (2016).

[8] P. Kehayias, M. J. Turner, R. Trubko, J. M. Schloss, C. A. Hart, M. Wesson, D. R. Glenn, and R. L. Walsworth, Imaging crystal stress in diamond using ensembles of nitrogen-vacancy centers, Phys. Rev. B **100**, 174103 (2019).

[9] Y. Schlussel, T. Lenz, D. Rohner, Y. Bar-Haim, L. Bougas, D. Groswasser, M. Kieschnick, E. Rozenberg, L. Thiel, A. Waxman, J. Meijer, P. Maletinsky, D. Budker, and R. Folman, Wide-Field Imaging of Superconductor Vortices with Electron Spins in Diamond, Phys. Rev. Appl. **10**, 034032 (2018).

[10] V. M. Acosta, E. Bauch, M. P. Ledbetter, C. Santori, K. M. Fu, P. E. Barclay, R. G. Beausoleil, H. Linget, J. F. Roch, F. Treussart, S. Chemerisov, W. Gawlik, and D. Budker, Diamonds with a high density of nitrogen-vacancy centers for magnetometry applications, Phys. Rev. B – Condens. Matter Mater. Phys. **80**, 115202 (2009).

[11] K. Ohno, F. Joseph Heremans, C. F. De Las Casas, B. A. Myers, B. J. Alemán, A. C. Bleszynski Jayich, and D. D. Awschalom, Three-dimensional localization of spins in diamond using ^{12}C implantation, Appl. Phys. Lett. **105**, 052406 (2014).

[12] C. Osterkamp, M. Mangold, J. Lang, P. Balasubramanian, T. Teraji, B. Naydenov, and F. Jelezko, Engineering preferentially-aligned nitrogen-vacancy centre ensembles in CVD grown diamond, Sci. Rep. **9**, 5786 (2019).

[13] T. R. Eichhorn, C. A. Mclellan, and A. C. Bleszynski Jayich, Optimizing the formation of depth-confined nitrogen vacancy center spin ensembles in diamond for quantum sensing, Phys. Rev. Mater. **3**, 113802 (2019).

[14] J. P. Tetienne, R. W. De Gille, D. A. Broadway, T. Teraji, S. E. Lillie, J. M. McCoey, N. Dontschuk, L. T. Hall, A. Stacey, D. A. Simpson, and L. C. Hollenberg, Spin properties of dense near-surface ensembles of nitrogen-vacancy centers in diamond, Phys. Rev. B **97**, 085402 (2018).

[15] E. E. Kleinsasser, M. M. Stanfield, J. K. Banks, Z. Zhu, W. D. Li, V. M. Acosta, H. Watanabe, K. M. Itoh, and K. M. C. Fu, High density nitrogen-vacancy sensing surface created via He^+ ion implantation of ^{12}C diamond, Appl. Phys. Lett. **108**, 202401 (2016).

[16] E. Bauch, C. A. Hart, J. M. Schloss, M. J. Turner, J. F. Barry, P. Kehayias, S. Singh, and R. L. Walsworth, Ultralong Dephasing Times in Solid-State Spin Ensembles via Quantum Control, Phys. Rev. X **8**, 031025 (2018).

[17] B. A. Myers, A. Ariyaratne, and A. C. Jayich, Double-Quantum Spin-Relaxation Limits to Coherence of Near-Surface Nitrogen-Vacancy Centers, Phys. Rev. Lett. **118**, 197201 (2017).

[18] H. J. Mamin, M. H. Sherwood, M. Kim, C. T. Rettner, K. Ohno, D. D. Awschalom, and D. Rugar, Multipulse Double-Quantum Magnetometry with Near-Surface Nitrogen-Vacancy Centers, Phys. Rev. Lett. **113**, 030803 (2014).

[19] G. De Lange, T. Van Der Sar, M. Blok, Z. H. Wang, V. Dobrovitski, and R. Hanson, Controlling the quantum dynamics of a mesoscopic spin bath in diamond, Sci. Rep. **2**, 382 (2012).

[20] F. Dolde, H. Fedder, M. W. Doherty, T. Nöbauer, F. Rempp, G. Balasubramanian, T. Wolf, F. Reinhard, L. C. Hollenberg, F. Jelezko, and J. Wrachtrup, Electric-field sensing using single diamond spins, Nat. Phys. **7**, 459 (2011).

[21] T. Mittiga, S. Hsieh, C. Zu, B. Kobrin, F. Machado, P. Bhattacharyya, N. Z. Rui, A. Jarmola, S. Choi, D. Budker, and N. Y. Yao, Imaging the Local Charge Environment of Nitrogen-Vacancy Centers in Diamond, Phys. Rev. Lett. **121**, 246402 (2018).

[22] V. M. Acosta, E. Bauch, M. P. Ledbetter, A. Waxman, L. S. Bouchard, and D. Budker, Temperature Dependence of the Nitrogen-Vacancy Magnetic Resonance in Diamond, Phys. Rev. Lett. **104**, 070801 (2010).

[23] D. A. Broadway, B. C. Johnson, M. S. Barson, S. E. Lillie, N. Dontschuk, D. J. McCloskey, A. Tsai, T. Teraji, D. A. Simpson, A. Stacey, J. C. McCallum, J. E. Bradby, M. W. Doherty, L. C. Hollenberg, and J. P. Tetienne, Microscopic imaging of the stress tensor in diamond using *in situ* quantum sensors, Nano Lett. **19**, 4543 (2019).

[24] K. Fang, V. M. Acosta, C. Santori, Z. Huang, K. M. Itoh, H. Watanabe, S. Shikata, and R. G. Beausoleil, High-Sensitivity Magnetometry Based on Quantum Beats in Diamond Nitrogen-Vacancy Centers, Phys. Rev. Lett. **110**, 130802 (2013).

[25] L. M. Pham, D. Le Sage, P. L. Stanwix, T. K. Yeung, D. Glenn, A. Trifonov, P. Cappellaro, P. R. Hemmer, M. D.

Lukin, H. Park, A. Yacoby, and R. L. Walsworth, Magnetic field imaging with nitrogen-vacancy ensembles, New J. Phys. **13**, 045021 (2011).

[26] J. M. McCoey, R. W. de Gille, B. Nasr, J. P. Tetienne, L. T. Hall, D. A. Simpson, and L. C. Hollenberg, Rapid, high-resolution magnetic microscopy of single magnetic microbeads, NanoMicroSmall **15**, 05159 (2019).

[27] A. M. Wojciechowski, M. Karadas, A. Huck, C. Osterkamp, S. Jankuhn, J. Meijer, F. Jelezko, and U. L. Andersen, Camera-limits for wide-field magnetic resonance imaging with a nitrogen-vacancy spin sensor, Rev. Sci. Instrum. **89**, 031501 (2018).

[28] See the Supplemental Material at http://link.aps.org/supplemental/10.1103/PhysRevApplied.15.054032 for further N-*V* ensemble and experimental setup details, the derivation of SQ, DQ, and DDQ signals, and fitting-model information.

[29] A. Gali, *Ab initio* theory of the nitrogen-vacancy center in diamond, Nanophotonics **8**, 1 (2019).

[30] A. Dréau, M. Lesik, L. Rondin, P. Spinicelli, O. Arcizet, J. F. Roch, and V. Jacques, Avoiding power broadening in optically detected magnetic resonance of single NV defects for enhanced dc magnetic field sensitivity, Phys. Rev. B—Condens. Matter Mater. Phys. **84**, 195204 (2011).

[31] S. Steinert, F. Ziem, L. T. Hall, A. Zappe, M. Schweikert, N. Götz, A. Aird, G. Balasubramanian, L. Hollenberg, and J. Wrachtrup, Magnetic spin imaging under ambient conditions with sub-cellular resolution, Nat. Commun. **4**, 1607 (2013).

[32] K. Sasaki, Y. Monnai, S. Saijo, R. Fujita, H. Watanabe, J. Ishi-Hayase, K. M. Itoh, and E. Abe, Broadband, large-area microwave antenna for optically detected magnetic resonance of nitrogen-vacancy centers in diamond, Rev. Sci. Instrum. **87**, 053904 (2016).

[33] M. W. Doherty, F. Dolde, H. Fedder, F. Jelezko, J. Wrachtrup, N. B. Manson, and L. C. Hollenberg, Theory of the ground-state spin of the NV-center in diamond, Phys. Rev. B—Condens. Matter Mater. Phys. **85**, 205203 (2012).

[34] L. Finzi and J. Gelles, Measurement of lactose repressor-mediated loop formation and breakdown in single DNA molecules, Science **267**, 378 (1995).

[35] D. T. Kovari, Y. Yan, L. Finzi, and D. Dunlap, Tethered Particle Motion: an easy technique for probing DNA topology and transcription factor interactions, Methods Mol. Biol. **1665**, 317 (2018).

[36] I. Fescenko, A. Laraoui, J. Smits, N. Mosavian, P. Kehayias, J. Seto, L. Bougas, A. Jarmola, and V. M. Acosta, Diamond Magnetic Microscopy of Malarial Hemozoin Nanocrystals, Phys. Rev. Appl. **11**, 034029 (2019).

[37] M. Gould, R. J. Barbour, N. Thomas, H. Arami, K. M. Krishnan, and K. M. C. Fu, Room-temperature detection of a single 19 nm super-paramagnetic nanoparticle with an imaging magnetometer, Appl. Phys. Lett. **105**, 072406 (2014).

[38] C. A. Hart, J. M. Schloss, M. J. Turner, P. J. Scheidegger, E. Bauch, and R. L. Walsworth, NV-Diamond Magnetic Microscopy Using a Double Quantum 4-Ramsey Protocol, Phys. Rev. Appl. **15**, 044020 (2020).